

On particle fountains in a crossflow

Eric L. Newland^{1,†} and Andrew W. Woods¹

¹Institute of Energy and Environmental Flows, Department of Earth Science, University of Cambridge, Madingley Road, Cambridge CB3 0EZ, UK

(Received 16 November 2022; revised 6 April 2023; accepted 18 April 2023)

We present new experiments of particle-laden turbulent fountains in a uniform horizontal crossflow, u_a , with momentum flux, M_0 , and buoyancy flux, B_0 . We use the ratio, P , of the crossflow speed to the characteristic fountain speed, $M_0^{-1/4}|B_0|^{1/2}$, and the ratio U , of the Stokes fall speed of the particles, v_s , to the characteristic fountain speed, to characterise the dynamics of a particle fountain in a crossflow. We find that the dynamics of these particle fountains can be categorised into three distinct regimes. In regime I when the fall speed of the particles is small in comparison with the characteristic fountain speed ($U \ll 1$), the particles remain well-coupled to the fountain fluid and the flow essentially behaves as a single-phase fountain in a crossflow. In the transitional regime II ($0.1 < U < 1$), when the fall speed of particles is comparable to the characteristic fountain speed, we observe some particles separating from the fountain fluid during the descent of the flow which leaves some fluid neutrally buoyant. As $U > 1$ (regime III), we observe particles separating from the fountain as it rises from the source. We measure the average dispersal distance of the particles and the speed of the descending particles as a function of U and P and compare these results with models of a single-phase fountain in a crossflow. We build a regime diagram to describe the effect of U and P on the flow dynamics and consider our work in the context of deep-submarine volcanic eruptions.

Key words: particle/fluid flow

1. Introduction

1.1. Background

The release of particle-laden fluid into the environment occurs in many settings, including both subaerial and subaqueous explosive volcanic eruptions (Head & Wilson 2003; Woods 2010; Newland, Mingotti & Woods 2022; Rowell *et al.* 2022) and tailings discharge from

† Email address for correspondence: eln36@cam.ac.uk

vessels during deep-sea mining (Mingotti & Woods 2020). The conditions of the ambient environment, such as density stratification and the presence of local crossflows, play a critical role in controlling the dynamics of these multiphase flows. Such conditions will have a significant effect on the dispersal distance of particles and the final location of the fluid in the flow, parameters which are both considered environmentally and economically important.

Geophysical flows are often more dense than the ambient fluid they interact with, due to the presence of dissolved or entrained material, and if the flow issues from a localised source and the buoyancy of the flow opposes the momentum of the flow, it will behave as a turbulent fountain (Hunt & Burridge 2015). Following the classical work on single-phase turbulent fountains (Morton, Taylor & Turner 1956; Turner 1966), there have been numerous experimental studies (Turner 1973; Baines, Turner & Campbell 1990; Zhang & Baddour 1998; Kaye & Hunt 2006; Williamson *et al.* 2008; Burridge & Hunt 2012) that describe the rise and subsequent collapse of these flows. These observations are further complemented by a suite of theoretical models (McDougall 1981; Bloomfield & Kerr 2000; Mehaddi *et al.* 2015) that build on the entrainment assumption of Morton *et al.* (1956), and find that for a turbulent fountain the entrainment coefficient $\alpha = 0.085 \pm 0.01$.

Mingotti & Woods (2016) carried out a detailed experimental study into particle-laden turbulent fountains in a homogeneous environment and showed that the dynamics of the two-phase flow is dependent on the ratio of the fall speed of the entrained particles, v_s , to the characteristic speed of the fountain, u_f ,

$$U = \frac{v_s}{u_f}, \quad (1.1)$$

where

$$u_f = M_0^{-1/4} |B_0|^{1/2} \quad (1.2)$$

is a function of the source momentum flux, M_0 , and the magnitude of the source buoyancy flux, $|B_0|$. The authors demonstrated that when $U \ll 1$, a particle-laden fountain behaves essentially as a classical single-phase fountain. However, for $U \sim 1$, the particles separate from the flow during the fountains ascent and settle to the floor, leaving the remaining fountain fluid positively buoyant which then rises as a plume. Using similar experimental techniques, Carazzo, Kaminski & Tait (2015) and Newland *et al.* (2022) investigated the effect of particle-sedimentation in turbulent fountains on the dynamics of volcanic eruption columns.

In many natural environments, for example the atmosphere or ocean, turbulent flows may interact with lateral crossflows, with magnitude u_a , that occur in the ambient fluid. There have been numerous investigations into the complex interaction between negatively buoyant single-phase fountains with a uniform crossflow (Taherian & Mohammadian 2021). Early studies, with a focus on the dilution of brine when discharged into estuaries (Anderson, Parker & Benedict 1973; Pincince & List 1973), presented extensive experimental data on jets that were both perpendicular and at an angle to a crossflow. Integral models were used to estimate the centreline location and average dilution of the flow, however Anderson *et al.* (1973) concluded that the models were only able to predict trends in the data rather than exact dilution profiles. Subsequently, by developing a model of forced plumes in a crossflow (Chu & Goldberg 1974), Chu (1975) introduced a mechanistic model for the motion and dilution of dense jets in a crossflow. This model, based on the assumption that the horizontal velocity of the fountain, u , quickly adjusts to the speed of the local crossflow, produced centreline trajectories that showed good agreement with the experimental data presented. Further detailed experimental studies

On particle fountains in a crossflow

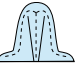
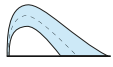
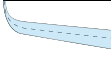
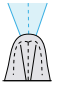
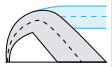
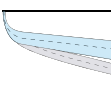
	Fountains		Plumes
	No wind	Wind	Wind
Single phase	<ul style="list-style-type: none"> • Turner (1966, 1973) • Bloomfield & Kerr (2000) • Burridge & Hunt (2012, 2013) • Kaye & Hunt (2016) 	<ul style="list-style-type: none"> • Pincince & List (1974) • Chu (1975) • Roberts & Toms (1987) • Gungor & Roberts (2009) • Ansong <i>et al.</i> (2011) 	<ul style="list-style-type: none"> • Hoult (1969) • Hewett <i>et al.</i> (1970) • Woodhouse <i>et al.</i> (2013) • Aubry <i>et al.</i> (2017) 
Particle laden	<ul style="list-style-type: none"> • Mingotti & Woods (2016) 	<div style="text-align: center; padding: 5px;">Present study</div> 	<ul style="list-style-type: none"> • James <i>et al.</i> (2022) • Mingotti & Woods (2022) 

Figure 1. Summary of major works on turbulent flows in a crossflow.

(Roberts & Toms 1987; Gungor & Roberts 2009; Choi, Lai & Lee 2016; Ben Meftah *et al.* 2018) qualitatively and quantitatively summarised the general characteristics of single-phase fountains in a crossflow as a function of the dimensionless crossflow Froude number, $Fr_a = (\pi/4)^{1/4} u_a/u_f$. Ansong, Anderson-Frey & Sutherland (2011) extended the Lagrangian theory for fountains in a stationary fluid to predict the centreline and radius of a fountain in a one- and two-layer crossflow. Their model assumes that the momentum flux at the source is predominantly vertical and therefore is only valid for sufficiently small crossflows.

It should also be noted that there is a significant body of literature on both single-phase and particle-laden plumes in a crossflow, initiated by the foundational work of Hoult, Fay & Forney (1969), Hewett, Fay & Hoult (1971) and Slawson & Csanady (1967), in which the authors developed models that trace the motion of the centreline of single-phase flows. Comprehensive studies into the entrainment of ambient fluid into such flows have since been carried out with a specific focus on volcanic plumes (Degruyter & Bonadonna 2013; Woodhouse *et al.* 2013; Aubry *et al.* 2017; Michaud-Dubuy, Carazzo & Kaminski 2020). James, Mingotti & Woods (2022) investigated the effect of particle sedimentation on the structure of particle-laden plumes in a crossflow and Mingotti & Woods (2022) extended this study by exploring the effect of varying the buoyancy of the interstitial fluid on the dynamics of such flows.

There has been significantly less attention paid to particle-laden fountains in a uniform crossflow. Fan, Xu & Wang (2010) and Park & Park (2021) measured the detailed structure and particle concentration in particle-laden jets, with the latter focusing on the influence of counter-rotating vortex pairs on particle dispersion in the flow. However, they did not compare the transport of the particles with the predictions of the Chu-type models of jets in a cross-flow in order to predict particle transport and deposition distances. Here we develop a series of new experiments to compare the predictions of these single-phase models with new experimental data. Figure 1 summarises the major works in this field.

1.2. Dimensionless scalings

Throughout this paper, the fountains we consider have a source Froude number, $Fr \gg 1$, where

$$Fr = \frac{M_0^{3/4}}{r_0 |B_0|^{1/2}} \propto \frac{u_0}{\sqrt{r_0 |g'_0|}} \quad (1.3)$$

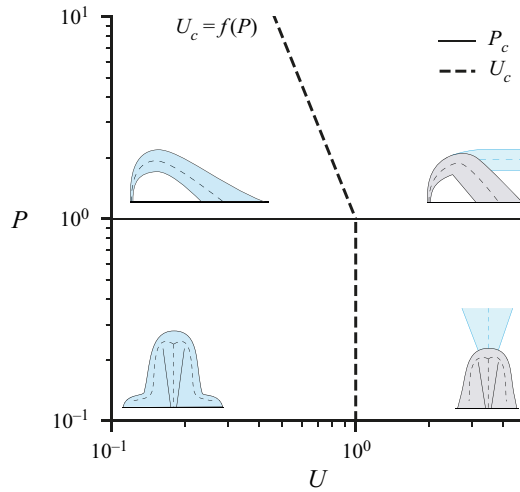


Figure 2. Dynamical regimes of particle-laden fountains in a crossflow as a function of the dimensionless fall speed of the particles, U , and dimensionless crossflow speed, P . The subscript c refers to the critical value of U at which particle separation affects the dynamics of the flow.

and u_0 , r_0 and g'_0 are the source speed, radius and buoyancy, respectively. This condition ensures that the momentum carries the flow vertically a greater distance than the scale of the source and, hence, the dynamics of the fountain are strongly influenced by turbulent entrainment (Morton *et al.* 1956; Burrige & Hunt 2012; Hunt & Burrige 2015), such that the top height of the fountain scales as

$$h_f = M_0^{3/4} |B_0|^{-1/2}. \tag{1.4}$$

In the case that a forced fountain is rising through an ambient crossflow, there is an additional length scale to consider (Hoult *et al.* 1969; Hoult & Weil 1972; Roberts & Toms 1987; Gungor & Roberts 2009; Devenish *et al.* 2010b), the jet adjustment length, h_m , that describes the height over which the speed of the fountain decreases to a value that is comparable to the speed of the crossflow:

$$h_m = \frac{M_0^{1/2}}{u_a}. \tag{1.5}$$

The ratio of the buoyancy-controlled length scale, h_f , to the jet adjustment length scale, h_m , provides a measure of the effect of the crossflow on the dynamics of a fountain. We define this ratio as

$$P = \frac{h_f}{h_m} = \frac{u_a}{u_f}. \tag{1.6}$$

When $P < 1$ the speed of the crossflow is small in comparison with characteristic fountain speed, and therefore the height of the fountain is limited by the source momentum and buoyancy fluxes and the ascent of the fountain is close to vertical. As the crossflow speed increases ($P > 1$), the fountain is bent over and the jet adjustment length decreases as u_a^{-1} (1.5) until h_m becomes the limiting length scale of the height of the fountain.

To assess the effect of particle size on the dynamics of the particle fountains in a crossflow, we adopt the approach of Mingotti & Woods (2016) and use the dimensionless

On particle fountains in a crossflow

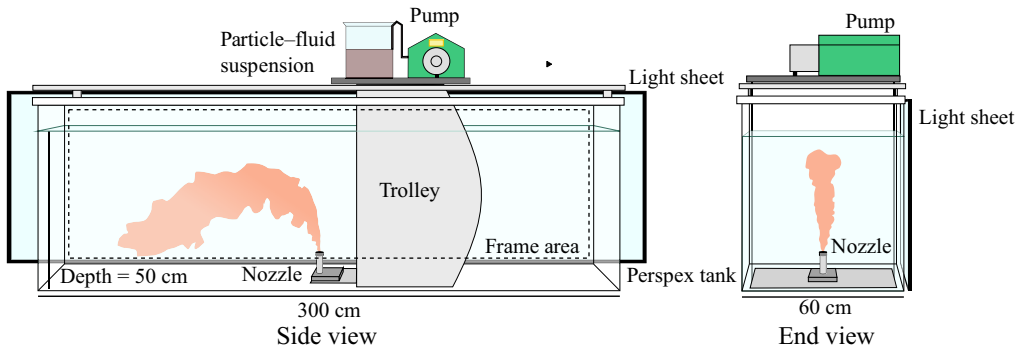


Figure 3. Experimental set-up.

fall speed of the particles, U (1.1). Similar to the dynamics of particle fountains in a stagnant homogeneous environment, when the crossflow speed is small in comparison with fountain speed ($P < 1$) we expect that for small particles ($U \ll 1$) the fountain will behave essentially as a single phase and for larger particles ($U > 1$), particle separation will dominate the dynamics of the flow. However, as the crossflow speed increases ($P > 1$) we anticipate that the critical value of U at which particle separation becomes important will be a function of the non-dimensional crossflow speed, P (figure 2). In this paper, we explore the effect of both U and P on the dynamics of these multiphase flows.

In § 2 of this study we describe the experimental set-up and image processing used throughout. We then present a set of reference experiments showing single-phase saline fountains injected from a moving source into a reservoir of fresh water and compare the data with the models developed in Chu (1975) and Ansong *et al.* (2011). Following this, we describe a series of experiments in which we form particle-laden fountains with neutrally buoyant interstitial fluid in a uniform crossflow and systematically vary the particle size and hence particle settling speed, v_s , and the crossflow speed, u_a . From these experiments, we identify three distinct regimes as a function of the dimensionless fall speed of the particles, U and investigate the effect of varying the crossflow speed on the point of transition between each regime. We present quantitative data on the fall speed of the particles and measure the average dispersal distance of the particles and compare these data with the model predictions of Chu (1975) to identify when particle separation effects become dominant. In § 5, we summarise the dynamics of these flows using a regime diagram and we consider the implications of this study for submarine volcanic eruptions.

2. Experimental set-up

To form small-scale negatively buoyant fountains in a uniform crossflow, we adopt an experimental approach used in earlier studies (Hoult *et al.* 1969; Chu & Goldberg 1974; James *et al.* 2022) and move a source at a constant speed through a static ambient environment; we expect this to be equivalent to a static source issuing a fluid into a uniformly flowing ambient. The experimental system consists of a large Perspex tank with length and width dimensions of 300 cm \times 60 cm (figure 3) filled with fresh or saline water to a depth of 50 cm. Fitted to the top of the tank is a track, along which a motorised trolley moves at constant speed. The saline solution or particle-fluid suspension that forms the fountain is supplied through a nozzle, with an inner diameter of 5 mm, located at the base of the trolley. The nozzle has an outer diameter of 2 cm and height of 5 cm (aspect

Exp.	M_0 ($\times 10^{-5}$)	Re	Fr	ρ_f	ρ_a	u_a ($\times 10^{-3}$)	P
a	2.00	3360	19	1057	1000	0.000	0.00
b	2.00	3360	19	1057	1000	0.003	0.05
c	2.00	3360	19	1057	1000	0.005	0.09
d	2.00	3360	19	1057	1000	0.006	0.12
e	2.00	3360	19	1057	1000	0.008	0.15
f	2.00	3360	19	1057	1000	0.008	0.16
g	2.00	3360	19	1057	1000	0.012	0.24
h	2.00	3360	19	1057	1000	0.015	0.30
i	2.00	3360	19	1057	1000	0.021	0.43
j	2.00	3360	19	1057	1000	0.031	0.61
k	2.00	3360	19	1057	1000	0.048	0.96
l	2.00	3360	19	1057	1000	0.075	1.52
m	2.00	3360	19	1057	1000	0.087	1.74
n	2.00	3360	19	1057	1000	0.138	2.77

Table 1. Experimental parameters for single-phase fountains in a uniform crossflow. Here M_0 ($\text{m}^4 \text{s}^{-2}$) is the source momentum flux, Re is the source Reynolds number, Fr is the source Froude number, ρ_f is the density of the fountain fluid (kg m^{-3}), ρ_a is the density of the ambient fluid (kg m^{-3}), u_a (m s^{-1}) is crossflow speed and P is the dimensionless crossflow speed.

ratio, $AR = 2.5$). Given the low AR of the nozzle, we do not expect there to be significant vortex shedding as a result of the flow around the nozzle and therefore do not expect that the dynamics of our fountain to be affected by the wake that forms behind the nozzle (Sumner, Heseltine & Dansereau 2004). The temperature of the injected and ambient fluid is measured and the variation between them is determined to be less than 0.5°C for each experiment. The arms of the trolley are sufficiently thin such that any wake produced by the trolley as it traverses along the tank does not have a measurable effect on the dynamics of the fountain. The speed of the trolley and, in turn, crossflow speed, u_a , is varied between experiments.

The particle–fluid suspension that forms the fountain consists of a dilute mixture of fresh water, with density $\rho_f = 1000 \text{ kg m}^{-3}$, and silicon carbide particles of density $\rho_m = 3206 \text{ kg m}^{-3}$ and major axis of length, d , in the range $22.8\text{--}212 \mu\text{m}$. For each particle size in our experiments, we estimate there to be a variation of size about the mean of, $\sigma \approx \pm 15\%$, calculated from the particle size range in Washington Mills SIC Particle Size Guide. Although the particles are not spherical, we use Stokes law to estimate the vertical fall speed of the particles, v_s , and control experiments carried out in previous studies (Mingotti & Woods 2019, 2020; Newland & Woods 2021) show that the measured values of the sedimentation speeds are in good agreement with the Stokes fall speed estimate. The dilute particle–fluid suspension, with particle volume concentration C_0 typically 2.5% , is stirred continuously and supplied to the injection nozzle using a Watson Marlow peristaltic pump at a constant volumetric flow rate, Q_0 . The source buoyancy flux of the mixture B_0 is given by

$$B_0 = \frac{\rho_a - \rho_m}{\rho_a} g Q_0, \tag{2.1}$$

where $\rho_m = C_0 \rho_p + (1 - C_0) \rho_f$ is the bulk density of the mixture and g is gravitational acceleration. The source Reynolds number, $Re = (u_0 r_0) / \nu_0$, where ν_0 is the kinematic viscosity of the source fluid, for each experiment is maintained above 2000 to ensure

Exp.	M_0 ($\times 10^{-5}$)	Re	Fr	C_0	D_p ($\times 10^{-6}$)	v_s ($\times 10^{-3}$)	U	u_a	P
1	2.00	2500	27	0.025	22.8	0.70	0.014	0.004	0.08
2	2.00	2500	27	0.025	22.8	0.70	0.014	0.054	1.11
3	2.00	2500	27	0.025	22.8	0.70	0.014	0.080	1.63
4	2.00	2500	27	0.025	22.8	0.70	0.014	0.106	2.16
5	2.00	2500	27	0.025	22.8	0.70	0.014	0.138	2.82
6	2.00	2500	27	0.025	44.5	2.68	0.055	0.045	0.92
7	2.00	2500	27	0.025	44.5	2.68	0.055	0.079	1.61
8	2.00	2500	27	0.025	44.5	2.68	0.055	0.098	2.01
9	2.00	2500	27	0.025	44.5	2.68	0.055	0.135	2.76
10	2.00	2500	27	0.025	63.0	5.35	0.11	0.005	0.09
11	2.00	2500	27	0.025	63.0	5.35	0.11	0.036	0.73
12	2.00	2500	27	0.025	63.0	5.35	0.11	0.061	1.25
13	2.00	2500	27	0.025	63.0	5.35	0.11	0.080	1.64
14	2.00	2500	27	0.025	63.0	5.35	0.11	0.135	2.76
15	2.00	2500	27	0.025	106	15.2	0.31	0.006	0.13
16	2.00	2500	27	0.025	106	15.2	0.31	0.018	0.36
17	2.00	2500	27	0.025	106	15.2	0.31	0.038	0.77
18	2.00	2500	27	0.025	106	15.2	0.31	0.065	1.33
19	2.00	2500	27	0.025	106	15.2	0.31	0.126	2.58
20	2.00	2500	27	0.025	125	21.2	0.43	0.005	0.10
21	2.00	2500	27	0.025	125	21.2	0.43	0.039	0.79
22	2.00	2500	27	0.025	125	21.2	0.43	0.059	1.21
23	2.00	2500	27	0.025	125	21.2	0.43	0.078	1.59
24	2.00	2500	27	0.025	125	21.2	0.43	0.129	2.63
25	2.00	2500	27	0.025	150	30.5	0.62	0.005	0.13
26	2.00	2500	27	0.025	150	30.5	0.62	0.022	0.45
27	2.00	2500	27	0.025	150	30.5	0.62	0.032	0.66
28	2.00	2500	27	0.025	150	30.5	0.62	0.061	1.26
29	2.00	2500	27	0.025	150	30.5	0.62	0.129	2.63
30	2.00	2500	27	0.025	180	43.9	0.90	0.034	0.69
31	2.00	2500	27	0.025	180	43.9	0.90	0.066	1.34
32	2.00	2500	27	0.025	180	43.9	0.90	0.078	1.58
33	2.00	2500	27	0.025	180	43.9	0.90	0.127	2.59
34	2.00	2500	27	0.025	212	60.8	1.24	0.006	0.12
35	2.00	2500	27	0.025	212	60.8	1.24	0.036	0.73
36	2.00	2500	27	0.025	212	60.8	1.24	0.067	1.37
37	2.00	2500	27	0.025	212	60.8	1.24	0.085	1.74
38	2.00	2500	27	0.025	212	60.8	1.24	0.123	2.51
39	2.00	3183	40	0.021	212	60.8	1.81	0.063	1.90
40	2.00	3183	54	0.016	212	60.8	2.43	0.062	2.51

Table 2. Experimental parameters for particle fountains in a uniform crossflow. Here M_0 ($\text{m}^4 \text{s}^{-2}$) is the source momentum flux, Re is the source Reynolds number, Fr is the source Froude number, C_0 is the initial concentration of particles in the fountain mixture, D_p (m) is the particle diameter, v_s (m s^{-1}) is the particle sedimentation speed, U is the dimensionless particle fall speed, u_a (m s^{-1}) is crossflow speed and P is the dimensionless crossflow speed.

the flow is turbulent. An electroluminescent light sheet (LightTape by Electro-LuminiX Lighting Corp.) is used to provide uniform lighting from one side of the tank and each experiment is filmed from a distance of 5 m using a Nikon D5300 digital camera at frame rate of 50 Hz. The frames captured in each experiment are analysed using MATLAB to extract bulk properties of the flow. Tables 1 and 2 display the conditions for each experiment.

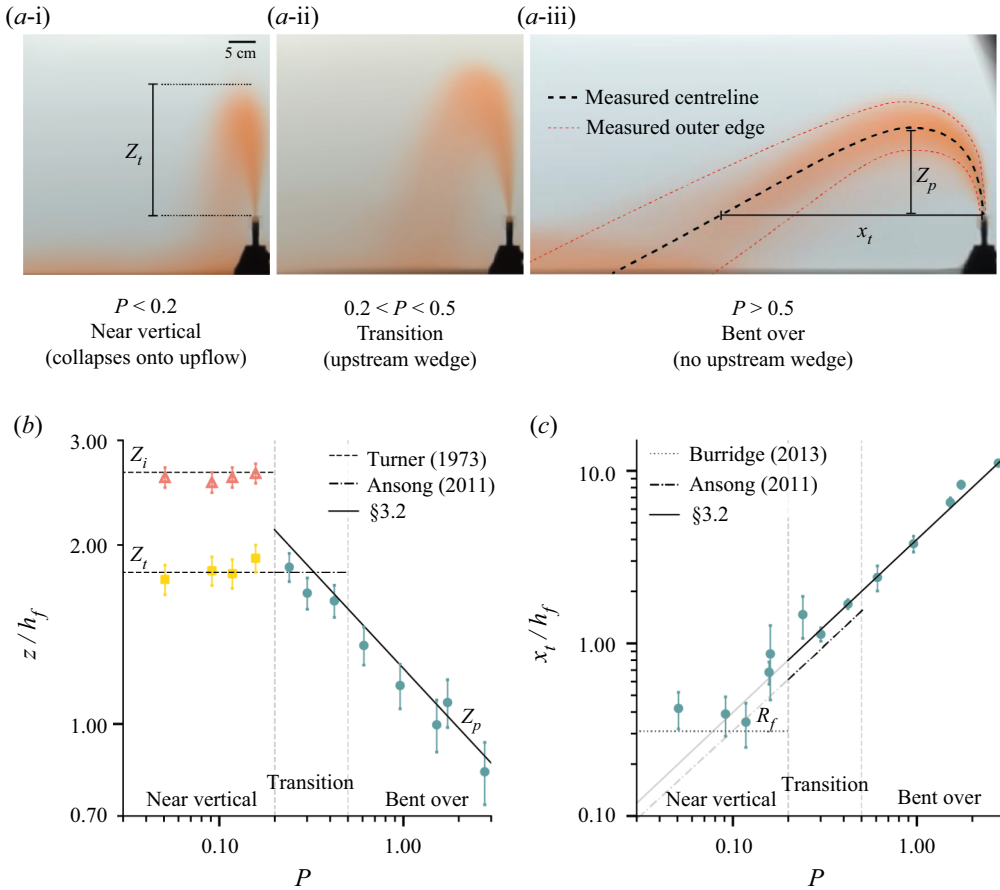


Figure 4. (a) Synthetic time-averaged images from (i) experiment d, (ii) experiment g and (iii) experiment k in table 1, displaying the three morphological regimes observed as a function of P . The fountain top height z_t is shown in (i) and the touchdown distance and maximum height of the fountain centreline is shown in (iii) alongside the measured fountain centreline and outer edge. (b) The measured height of a fountain in a crossflow as a function of P . The red triangles represent the transient initial height, z_t , only observable when $P < 0.2$, the yellow squares represent the steady-state top height, z_t (as shown in (a-i)), and the green circles represent the maximum height of the centreline, z_p (as shown in (a-iii)). The dashed horizontal lines show the estimates of the initial and top height of fountain in a stagnant environment (Turner 1973), the dot-dashed and solid lines show the model estimates of the maximum height of the fountain centreline from Ansong *et al.* (2011) and Chu (1975), respectively. (c) The measured touchdown distance, x_t , as a function of the dimensionless variable P . The horizontal dashed line indicates the estimate of the maximum radius of a fountain in a stagnant environment, R_f , as defined by Burrige & Hunt (2013). The dot-dashed and solid lines show the model estimates of the touchdown distance, x_t , from Ansong *et al.* (2011) and Chu (1975) respectively. The vertical dashed lines in (b,c) represent the morphological regimes as a function of P , described in § 3.1.

3. Single-phase fountains in a crossflow

3.1. Experimental observations

Figure 4(ai-iii) shows a series of time-averaged experimental images of single-phase saline fountains with the same initial momentum, M_0 , and buoyancy flux, B_0 , but with increasing crossflow speed, u_a . From these time-averaged images, we isolated the vertical distribution of dye concentration along each vertical line through the fountain and fit a Gaussian distribution to these profiles. Using the position of the maximum and standard deviation of this Gaussian fit, we obtained an estimate of the centreline and outer edges of

the fountain, as shown in figure 4(a-ii). Figure 4(b) presents the measured and theoretical heights of a fountain as a function of P . For $P < 0.2$, the transient initial, z_i and steady state, z_t , of the fountain are presented and for $P > 0.2$, the maximum height of the fountain centreline is presented. Figure 4(c) presents the measured and theoretical distance at which the centre of mass of the fountain passes the nozzle height (the touchdown distance, x_t), as shown in figure 4(a-iii). Based on the morphology of these fountains we have characterised the flows as a function of P into three regimes (Roberts & Toms 1987; Gungor & Roberts 2009).

In the case of a weak crossflow, $P = 0-0.2$, the fountain is only slightly deflected as it rises from the nozzle. The fountain entrains ambient fluid during its initial ascent which leads to an increase in the radius of the flow, until it reaches a maximum height, z_t . The fountain then collapses and, as it is only slightly deflected, interacts and entrains fluid from the upflowing region. Similar to a fountain in a stagnant homogeneous environment, the interaction between the upflow and downflow causes a reduction in the top height of the fountain to a steady-state value z_t . As shown in figure 4(b), in the region $P = 0-0.2$, an initial height z_i and steady-state height z_t can be measured and the values are in agreement with the classical scalings of Turner (1966) for single-phase fountains in a stagnant environment. As the fountain collapses back on itself, we expect that the touchdown distance, x_t , is comparable to the width of the fountain at the maximum height. For comparison, we have plotted a scaling for the maximum radius of a fountain, R_f , as predicted by Burrige & Hunt (2013), that provides a lower limit for the touchdown distance of the fountain as $P \sim 0$.

As the speed of the crossflow increases so that P lies in the range 0.2–0.5, the steady-state height of the fountain increases as, owing to the larger deflection of the fountain, the collapsing region of the flow no longer interacts with nor entrains fluid from the upflowing region. In addition, the transient initial height visible for fountains when $P < 0.2$ is no longer observed and the touchdown distance of the fountain increases (figure 4c). Figure 4(a-iii) illustrates the case when $P > 0.5$ and the crossflow speed is comparable to characteristic speed of the fountain. The fountain displays a decrease in the steady top height, z_t , and an increase in the touchdown distance, x_t , as P increases.

3.2. Modelling

A number of models have been proposed to describe single-phase fountains in a uniform crossflow. In figure 4(b,c) we present the estimates for the fountain top height, z_p , and touchdown distance, x_t , from models developed by Ansong *et al.* (2011), for low-moderate crossflow speeds, and Chu (1975), for moderate-high crossflow speeds. Ansong *et al.* (2011) extend the Lagrangian theory for fountains in stationary environments (Lee & Chu 2003) and assume that the momentum flux near the source is predominately vertical and therefore neglect the development of streamwise vorticity. Although the model does not account for the reduction in z_p that is observed as the crossflow speed increases, when $P = 0.2-0.5$ the measured values of z_p and x_t in figure 4 show reasonable agreement with the model estimates.

For moderate-high crossflow speeds, the flow becomes blown over by the effective ambient flow (in the frame of the jet) and so the entrainment and mixing is dominated by the tilted fountain dynamics, which includes the effect of the coherent axial vorticity, rather than the vertical fountain dynamics, where the entrainment is smaller. To illustrate the transition between a vertical fountain and a bent-over fountain, figure 5 shows the vertical momentum flux of a fountain at the height at which the upward speed is equal to the crossflow speed, \hat{M} , calculated using the model presented in Ansong *et al.* (2011),

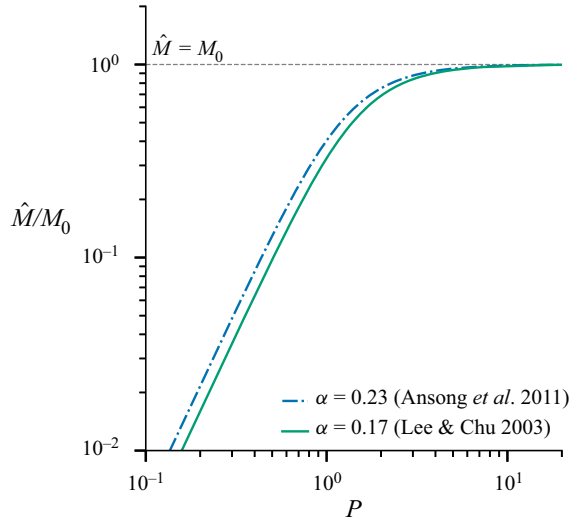


Figure 5. The ratio of the momentum flux of a fountain at the height at which the upward speed is equal to the crossflow speed, \hat{M} , to the initial vertical momentum flux, M_0 , calculated using the model presented in Ansong *et al.* (2011), as a function of the dimensionless crossflow speed, P . The different curves represent the model results using the best-fit values of the entrainment coefficient from Ansong *et al.* (2011) and Lee & Chu (2003).

as a function of the dimensionless crossflow speed, P . For a fountain to be controlled by the bent-over fountain dynamics, the horizontal speed of the fountain should adjust to the crossflow speed while the upward momentum flux is still of comparable size to \hat{M} . Figure 5 shows that this transitions occurs in the region $P \sim 1$.

For a fountain in this regime, Chu (1975) introduced a mechanistic model, based on the assumptions that the horizontal component of the fountain velocity, u , is equal to the crossflow speed, u_a , and using conservation of mass and momentum for the vertical flow at each point along the jet, including a simple parameterisation of the entrainment. A similar approach has also been used to describe the trajectory of buoyant plumes in a crossflow (Hoult *et al.* 1969; Hewett *et al.* 1971; James *et al.* 2022). Given the assumption that $u = u_a$, the horizontal position of the fountain centreline is given by

$$\frac{dx}{dt} = u_a. \tag{3.1}$$

The fountain fluid has a vertical speed defined as $w = dz/dt$ and a characteristic radius, r , perpendicular to the direction of the crossflow. The entrainment of ambient fluid leads to an increase in the radius of the fountain with height (Hewett *et al.* 1971; Chu & Goldberg 1974)

$$\frac{dr}{dz} = \alpha, \tag{3.2}$$

where α is an entrainment coefficient. As the buoyancy flux along the fountain remains constant in a homogeneous environment, the vertical momentum in each element of the fountain develops as it moves downstream

$$\frac{d(\pi r^2 w)}{dt} = \gamma \pi r^2 g', \tag{3.3}$$

where g' is the reduced gravity of the fountain fluid and γ is a coefficient used to account for the momentum that is associated with any circulation in the fountain fluid, in addition

On particle fountains in a crossflow

to the added mass of ambient fluid that is displaced as the fountain rises and falls. Given the source buoyancy flux takes value B_0 this can be expressed as

$$\frac{d(\pi r^2 w)}{dt} = -\frac{\gamma |B_0|}{u_a} \tag{3.4}$$

which leads to the relation

$$\pi r^2 w = (\pm) \gamma \left(\frac{|B_0|}{u_a} t + \frac{M_0}{u_a} \right). \tag{3.5}$$

In the momentum equation, we have included the factor of γ in front of the source momentum term as well, as the initial source momentum is partitioned into the upward flow, the circulation and the added mass, which are not present in the vertical flow leaving the nozzle. Using (3.2), we integrate (3.5) with the negative sign with respect to time to obtain the expressions for the height of the fountain above the source, z_u , for the ascending fountain

$$\left. \begin{aligned} z_u^3 &= \left(\frac{3\gamma}{\pi\alpha^2} \right) \left(-\frac{1}{2} \frac{h_m^3}{h_f^2} x^2 + h_m^2 x \right) \\ r_u^3 &= \left(\frac{3\gamma\alpha}{\pi} \right) \left(-\frac{1}{2} \frac{h_m^3}{h_f^2} x^2 + h_m^2 x \right) \end{aligned} \right\}, \quad \text{as } x < x_p, \tag{3.6}$$

where the transform $x = u_a t$ has been used and h_m and h_f are the jet adjustment and buoyancy controlled length scales, as defined in § 1 and x_p is the horizontal distance to the peak of the fountain where

$$\frac{dz_u^3}{dx} = 0 \tag{3.7}$$

and therefore the distance, x_p , and height, z_p , at the maximum height of the fountain are given by

$$x_p = \frac{h_f^2}{h_m}, \quad z_p = \left(\frac{3\gamma}{2\pi\alpha^2} \right)^{1/3} (h_m h_f^2)^{1/3}, \quad r_p = \alpha z_p. \tag{3.8a-c}$$

For the descending plume which develops downstream from this point, using the positive sign we integrate (3.5) with respect to time to give expressions for the height above the source, z_d ,

$$\left. \begin{aligned} 2z_p^3 - (2z_p - z_d)^3 &= \left(\frac{3\gamma}{\pi\alpha^2} \right) \left(-\frac{1}{2} \frac{h_m^3}{h_f^2} x^2 + h_m^2 x \right) \\ 2r_p^3 - r_d^3 &= \left(\frac{3\gamma\alpha}{\pi} \right) \left(-\frac{1}{2} \frac{h_m^3}{h_f^2} x^2 + h_m^2 x \right) \end{aligned} \right\}, \quad \text{as } x > x_p. \tag{3.9}$$

By differentiating equations (3.6) and (3.9) with respect to time, we obtain expressions for the vertical component of the fountains velocity in the upflowing

$$w_u = \left(\frac{\gamma}{9\pi\alpha^2} \right)^{1/3} \left(-\frac{1}{2} \frac{h_m^3}{h_f^2} x^2 + h_m^2 x \right)^{-2/3} \left(-\frac{h_m^3 u_a}{h_f^2} x + h_m^2 u_a \right), \tag{3.10}$$

and downflowing regions of the fountain

$$w_d = - \left(\frac{\gamma}{\pi\alpha^2} \right) \left[2z_p^3 - \left(\frac{3\gamma}{\pi\alpha^2} \right) \left(-\frac{1}{2} \frac{h_m^3}{h_f^2} x^2 + h_m^2 x \right) \right]^{-2/3} \left(-\frac{h_m^3 u_a}{h_f^2} x + h_m^2 u_a \right). \quad (3.11)$$

3.3. Entrainment coefficient

To obtain a value of the entrainment coefficient, α , we measured the spreading rate of the initial rise of the fountain as a function of height for experiments in which $P > 1$. As described in § 3.1, we measure the radius of the fountain by fitting a Gaussian curve to vertical dye profiles taken along the length of the fountain and define the outer-edges of the fountain as a standard deviation, σ , away from the centre of mass. We find the relationship

$$\sigma = (0.25 \pm 0.03)z, \quad (3.12)$$

and therefore, if we define the fountain radius as equal to the standard deviation, we find that

$$\frac{d\sigma}{dz} = \alpha = 0.25 \pm 0.03. \quad (3.13)$$

This value for the entrainment coefficient is consistent with that obtained by Ansong *et al.* (2011) who find that for a fountain in a slow-moderate crossflow, $\alpha = 0.23$. These estimates of the entrainment coefficient are larger than those obtained for other free shear flows because the flow at hand includes coherent axial vorticity in the form of a double vortex structure as the flow becomes progressively more horizontal while it rises or falls – this increases the entrainment. Although our value of the entrainment coefficient is smaller than the value obtained by Chu & Goldberg (1974) and Chu (1975), their formulation did not account for the added mass and circulation of the flow and their measurements of the radius in fact suggested that α has value of about 0.25 (Chu 1975) consistent with the present value.

Studies of turbulent buoyant plumes in a crossflow have found that, once the flow has fully developed, the spreading rate of the plume can be described using a value of the entrainment coefficient $\alpha = 0.4 - 0.6$ (Hoult *et al.* 1969; Hoult & Weil 1972; Chu & Lee 1996; Devenish, Rooney & Thomson 2010a; James *et al.* 2022). For a turbulent fountain in a crossflow, the descending region of the flow essentially behaves as a buoyant plume with an initial finite radius, r_p . However, at the peak of the fountain the flow includes significant circulation with an associated speed which we expect to scale with the bent-over fountain speed

$$u_c = \left(\frac{|B_0|^2}{M_0 u_a} \right)^{1/3}. \quad (3.14)$$

As the flow descends from the top of the fountain, we expect it will gradually adjust towards the classic self-similar plume in a cross-flow as described by Hoult *et al.* (1969), Hewett *et al.* (1971) and Slawson & Csanady (1967). In this adjusted flow, we expect that the circulation in the flow will scale with the mean flow; since the speed of a self-similar plume increases with vertical distance according to the relation,

$$u_p = \left(\frac{|B_0|}{u_a} \right)^{1/2} z^{-1/2}, \quad (3.15)$$

it follows that the adjustment will require a distance which scales with the height of the fountain. Thus during the descent the flow will be in transition, and the entrainment may

be intermediate between the fountain and the plume like flow regimes. Comparison of the model with our experimental data suggest that the entrainment coefficient $\alpha = 0.25 \pm 0.03$ and added mass coefficient $\gamma = 0.25$ provides the best fit to the data; these are smaller than the values for the adjusted self-similar plume, $\alpha = 0.4$ and $\gamma = 0.47$ (James *et al.* 2022) and so we adopt these in the present analysis.

Figure 4(b,c) presents the model estimates of the maximum height, z_p , and the touchdown distance, x_t , of the fountain respectively. The measured values of the maximum height show good agreement with the model estimates as $P > 1$ and the model estimates of the touchdown distance, x_t , slightly over predicts the measured values, however follows the same trend.

4. Particle fountains with neutrally buoyant fluid

4.1. Qualitative observations

We now present a series of experiments exploring the dynamics of particle-laden fountains with neutrally buoyant interstitial fluid and the effect of varying the dimensionless fall speed of the particles, U , and the dimensionless crossflow speed, P (table 2). Figure 6 displays images from experiments 2, 17, and 36 and highlights the three qualitative regimes identified in this study to describe the dynamics of particle fountains in a crossflow. For comparison of these three regimes we have presented instantaneous experimental images, time-averaged images with the backgrounds subtracted and the model estimates of the mean centreline and radius superimposed (3.6) and (3.9) and a simplified schematic diagram highlighting the key observations.

Regime I describes the case when the fall speed of the particles is significantly slower than the characteristic speed of the fountain ($U \ll 1$). In this regime the particles in the mixture remain well coupled with the fountain fluid and the flow essentially behaves as a single-phase fountain. From the time-averaged image, we can see that the model estimates of the centreline and radius of a single-phase fountain show very good agreement with the morphology of the particle fountain in this regime. This observation is consistent with observations of similar flows in various studies (Mingotti & Woods 2016; Newland & Woods 2021; James *et al.* 2022).

As the size and the fall speed of the particles increase ($0.1 < U < 1.0$), the structure of the flow deviates from that of a single-phase fountain in a crossflow. In the instantaneous image for regime II, we can see that the particles and fountain fluid remain well mixed during the ascent of the fountain. The time-averaged image also shows that during the ascent of the fountain, the model predictions of the centreline and radius show good agreement with the experimental image. However as the mixture descends, there is some separation of particles from the mixture and in both the instantaneous and time-averaged images dyed red fluid is seen on the top-side of the flow whereas a dark region of particles is observed on the bottom-side of the flow. It is also evident that as the flow descends the trajectory of the mixture diverges from the single-phase model predictions and the dark region of particles reaches the base of tank more quickly than the prediction of a convecting flow.

Finally, as U increases towards a value of 1, the fall speed of the particles approaches the characteristic fountain speed. The experimental images demonstrate that, in regime III, the structure of the flow is substantially different to that of a single-phase fountain in a crossflow. The instantaneous image shows that during the initial rise of the fountain, particles begin to sediment from the base of flow and settle through the water column. As a result, the bulk density of the mixture is reduced and when all the particles have separated from the fluid, the fluid becomes neutrally buoyant and therefore does not collapse to the

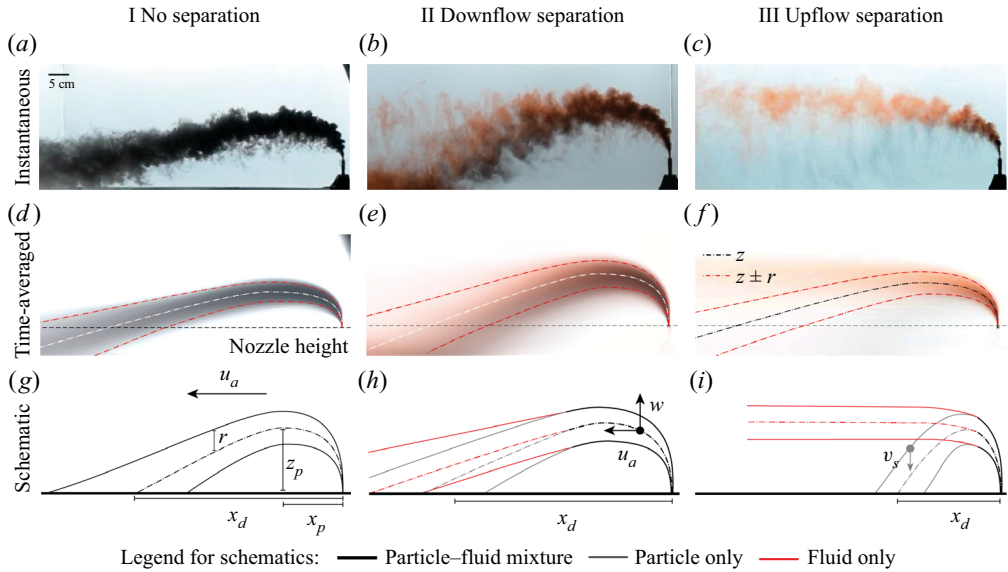


Figure 6. Selection of images from experiments 2, 17 and 36 showing the three separation regimes observed in particle-fountains in a uniform crossflow: I, no particle separation; II, particle separation on the downflow section of the fountain; and III, particle separation on the upflow section of the fountain. (a–c) displays instantaneous experimental images. (d–f) shows synthetic time-averaged images with the estimated centreline (white or black dashed lines), z , and outer edge (red dashed lines), $z \pm r$, for a single-phase fountain in a crossflow (3.6) and (3.9) superimposed. (g–i) displays schematic diagrams showing the variables used to describe particle-laden fountains in a crossflow: u_a , uniform crossflow speed; x_p , z_p , coordinates of maximum height of the fountain centreline (Chu 1975); r , characteristic radius of fountain; x_d , particle-dispersal distance; w , vertical speed of fountain; and v_s , vertical particle settling speed.

base of tank but instead rises slowly through the water column due to a residual component of vertical momentum. In the time-averaged image, a dark region of settling particles can be seen below the rising red region of fluid. The dispersal distance of the particles from the source is significantly shorter than the distance reached by a single-phase fountain.

Thus far, we have presented the qualitative effect of varying the particle size on the dynamics of particle-laden fountains in a crossflow. We will now explore the influence of the crossflow speed on the dynamics of these complex multiphase flows. Figure 7 displays instantaneous and time-averaged images from three experiments in which the particle size and therefore dimensionless fall speed is kept constant, $U = 0.62$, and the crossflow speed is varied. When the crossflow speed is small in comparison to the characteristic fountain speed, $P = 0.13$, it is noticeable, from the instantaneous and time-averaged images, that the majority of the red fountain fluid is transported to the base of the tank with the particles and only a small fraction of fluid remains at or above the maximum height of the fountain. This indicates that the particles do not completely separate from the fountain fluid and some particles remain coupled with the fluid during the fountains descent. However as the speed of the crossflow increases, $P = 0.66$, the fraction of fluid remaining at or above the maximum height of the fountain increases and the fraction collapsing to the base of the tank decreases. Furthermore as $P > 1$, we can see that only a very small fraction of the fountain fluid is transported to the base of the tank and the majority of the fluid remains at the maximum height of the fountain. This trend suggests that when $U = 0.62$ and the speed of the crossflow is increased, the fraction of particles that completely separate from the fountain fluid increases and therefore a larger fraction of fluid remains at a height

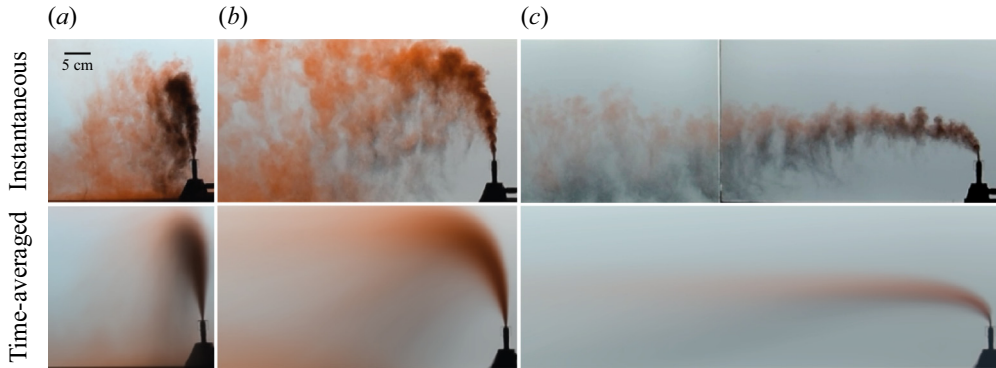


Figure 7. Instantaneous and time-averaged experimental images of particle-laden fountains with $U = 0.62$ and (a) $P = 0.13$ (experiment 25), (b) $P = 0.66$ (experiment 27) and (c) $P = 2.63$ (experiment 29).

comparable to the maximum height of the fountain rather than being carried back down to the base tank with the particles.

4.2. Quantitative results

As well as the qualitative observations presented above, we have measured the average vertical speed of the descending particles, v_m , and the average dispersal distances of the particles, x_d , as a function of U and P . Figure 8 displays the method and results of the analysis carried out to determine the vertical speed of the descending particles. Panels (a-i) and (a-ii) are synthetic time-series created by isolating a vertical line of pixels, in the reference frame of the experimental tank, for a set of frames taken during an experiment. In this image, the horizontal direction represents time and the vertical direction represents the height of the tank. Each time-series records the rise and fall of the particle fountain as it traverses past the line of pixels, and can be used to measure the vertical speed of the descending particles as they settle to the base of the tank. The vertical speed is estimated by calculating the gradient of the particle-streaks formed as the particles descend through the tank, using a Hough transform (shown by the green and red lines). To measure the average vertical speed of the descending particles, we created over 25 time-series for each experiment that were equally spaced throughout the duration of the experiment and sampled the whole width of the cloud of descending particles. We measured the vertical speed of the particles at a height in the tank that is comparable to the height of the nozzle and did not observe any systematic variation of our measurements throughout the duration of the experiments. The average vertical speed of the particles, v_m , is plotted in figure 8(b,c) as a function of the dimensionless fall speed, U . Each data point is coloured according to the value of the dimensionless crossflow speed, P , of the experiment. To clearly demonstrate the varying dynamics as a function of the dimensionless fall speed, U , and dimensionless crossflow speed, P , we use two independent scalings in figure 8(b,c).

In figure 8(b) we have scaled the measured vertical speed of the descending particles, v_m , with the modelled vertical speed of a single-phase fountain at the touchdown distance, $w_d(x = x_t)$ (3.11). We term this convective speed, v_c . By scaling our measured data, v_m , with v_c we can see that when $U < 0.1$, in the vertical direction the descending particles are moving close to the vertical single-phase convective speed for all values of P . These data corroborate our earlier observations that when $U \ll 1$, the particles remain well-mixed in the fountain and the flow essentially behaves as a single-phase (regime I). As U increases beyond 0.1, the measured vertical speed of the particles increases to values greater than the vertical component of the single-phase convective speed, v_c .

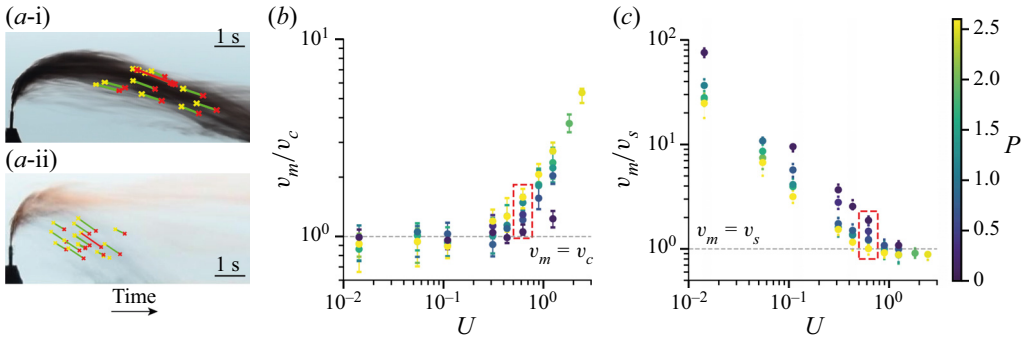


Figure 8. Analysis of the vertical speed of the descending particles. (a) Synthetic vertical time-series taken in the reference frame of the tank during an experiment where (i) $U < 1$ and (ii) $U > 1$. The superimposed green and red lines indicate streaks highlighted when using a Hough transform to measure the vertical speed of the descending particles. (b) The measured average vertical speed of the descending particles, v_m , scaled with the vertical speed of a single-phase fountain at the touchdown point, v_c , as calculated from (3.11). (c) The measured average vertical speed of the descending particles, v_m , scaled with Stokes fall speed of the particles, v_s . Each data point is coloured as a function of the measured dimensionless crossflow speed, P .

In figure 8(c) we have scaled the measured vertical speed of the descending particles, v_m , with the Stokes fall speed of the particles, v_s . This data shows that for $U \ll 1$ the particles are moving at vertical speeds that are much greater than their Stokes fall speed, and from figure 8(b) we know that this speed is comparable to the vertical component of the single-phase convective speed of the fountain, v_c . However as U increases beyond 1 we see that in the vertical direction the particles descend at a speed close to their Stokes fall speed, which suggests that the particles have separated from the flow and are settling through the water column (regime III). We have shown how these two scalings help reveal the dynamics of the two end-member regimes, in which either the particles remain well mixed in the flow and the fountain behaves essentially as a single-phase (regime I) or the particles completely separate from the fluid and settle through the water column at their Stokes fall speed (regime III). In addition, this data also helps to demonstrate the effect of varying crossflow speed on the separation dynamics of the particles. For example, by examining the results of v_m/v_c when $U = 0.62$ (red-dashed box in figure 8b) we see that for slow crossflow speed ($P < 1$, dark blue data point) the measured vertical speed of the particles is close to the vertical component of the single-phase convective speed at the touchdown distance, v_c , indicating that the particles remain coupled with the fountain fluid. However as the speed of the crossflow increases (green/yellow data points) the measured vertical speed of the particles increases to speeds significantly greater than the vertical component of the single-phase convective speed, v_c . By looking at the same data in figure 8(c) (red-dashed box), we see that for faster crossflow speeds (green/yellow data points) the measured vertical speed tends towards the Stokes fall speed of the particles, suggesting that the particles separate from the fluid and settle through the water column. This data verifies our observations in § 4.1, that although the particle size is kept constant, particles in a fountain in a faster crossflow speed tend to separate more completely than the particles in a fountain in a slower crossflow speed.

It is also of interest to measure the average dispersal distance of the particles, x_d , from the source. We define x_d as the horizontal distance from the source to the centre of mass of the descending particle cloud at the height of the nozzle (schematics in figure 6). Once again to highlight the varying dynamics of the particle fountains as a function of U and P , we present the measured dispersal distance scaled with two independent length-scales in figure 9(a,b) and have coloured each data point according to the corresponding value of P .

On particle fountains in a crossflow

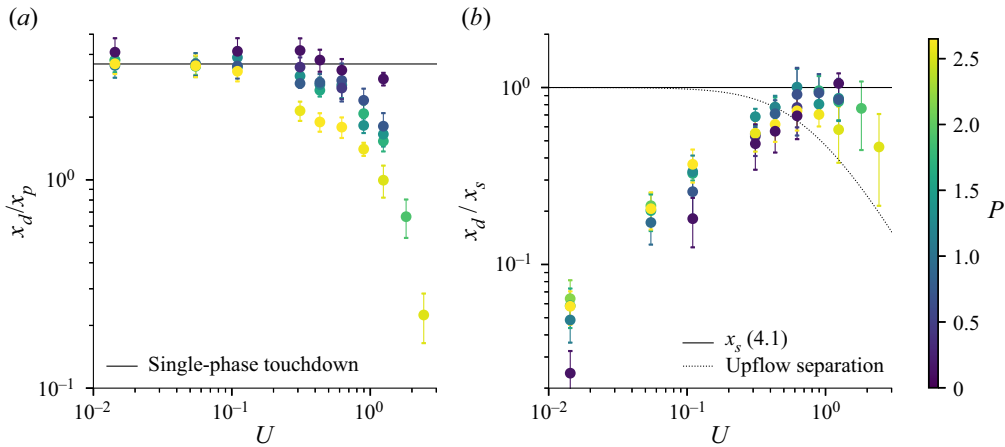


Figure 9. (a) The dispersal distance of the particles scaled with the distance to the peak of the fountain, x_p (3.8a–c), as a function of dimensionless fall speed of the particles, U . The black solid line represents the touchdown distance of a single-phase fountain as calculated from (3.9). (b) The dispersal distance of the particles scaled with the dispersal distance of a particle that separates from the peak of fountain and settles through the water column, x_s (4.1), as a function of dimensionless fall speed of the particles, U . The dotted line represents the dispersal distance a particle that separates from the flow during the ascent of the fountain at the point at which $w = v_s$. Each data point is coloured as a function of the measured dimensionless crossflow speed, P .

Figure 9(a) displays the average dispersal distance of the particles scaled with the horizontal distance to the peak of a single-phase fountain, x_p (3.8a–c). These data show that for $U < 0.1$, the average dispersal distance of the particles corresponds to the touchdown distance of a single-phase fountain, calculated from (3.6) and (3.9), for all values of P . As U increases beyond 0.1, we see that the dispersal distance of the particles decreases at a rate that is dependent on the crossflow speed, P . The decrease in the particle dispersal distance is due to the separation of particles from the flow and subsequent settling of those particles through the water column. For small values of P (dark blue points), x_d starts to decrease in the region $U \sim 1$, which is in contrast to large values of P where we observe a decrease in the particle dispersal distance as $U \sim 0.2$. This suggests that in the experiments with faster crossflow speeds, the particles begin to separate from the flow at smaller values of U . This observation is consistent with the data presented in figure 8, where we show that the speed of the descending particles is strongly dependent on the crossflow speed P .

To gain further insight into the separation and dispersal of the particles, we can consider the path a particle may follow in this flow. We have shown that as $U \ll 1$, the particles remain well-mixed in the fountain and follow the path of a single-phase fountain in a crossflow. Our qualitative and quantitative observations suggest that as U increases beyond 0.1, particles separate from the fountain during either the ascent or descent phase of the flow and settle at their Stokes fall speed through the water column. As a characteristic length scale for the horizontal distance travelled by a particle that separates from the fountain fluid, we may consider the case in which a particle remains coupled to the fountain fluid to the peak of the fountain, distance x_p from the source and height z_p above the source, and then separates from the flow and settles to the base of the tank at the Stokes fall speed of the particle, v_s . Assuming that the particle is always moving at the speed of the crossflow, u_a , in the horizontal direction, the distance travelled by the particle from the

source is given by

$$x_s = x_p + \frac{z_p u_a}{v_s}. \quad (4.1)$$

In [figure 9\(b\)](#) we have scaled the average particle dispersal distance, x_d , with this length scale. For $U \ll 1$, the average dispersal distance follows the single-phase touchdown distance and is significantly smaller than the ballistic trajectory, x_s . As $U \sim 1$, we see that for slow crossflow speed (blue points) the dispersal distance tends to x_s , which suggests that particle separation occurs near to the peak of fountain. However, as P increases (light green/yellow points), we see that the dispersal distance tends to x_s around $U = 0.6$, but then shows a rapid decrease as U continues to increase. We have shown that when $U \sim 1$ particles settle at their Stokes fall speed, and therefore the decrease in the particle dispersal distance must be a result of the particles separating from the fountain prior to reaching the peak of the fountain. As a simple estimate of the point of particle separation during the ascent of the fountain, using (3.10) ([figure 10](#)), we find the location at which the magnitude of the vertical velocity of the fountain is equal to the Stokes fall speed of a particle, $|w_u| = v_s$. Then following the above method, we assume that the particle remains well coupled to the fountain fluid until the condition $|w_u| = v_s$ is met, at which point the particle settles through the water column at its Stokes fall speed to the base of the tank. We have included this estimate of the dispersal distance in [figure 9\(b\)](#) (dotted line) using an average current speed from our experiments when $P > 1.5$. This condition acts a lower limit for the dispersal of particles that may separate during the ascent of the fountain. These data show that for $P > 1.5$, the data tend to this estimate. However, the bulk of the particles are dispersed further from the source.

5. Discussion

5.1. Regime diagram

In [§ 4](#), we have presented a set of qualitative and quantitative observations and introduced three distinct regimes to describe the dynamics of particle fountains in a crossflow. In regime I, when the dimensionless fall speed of the particles is small, $U \ll 1$, we show that the particles remain well coupled to the fountain fluid and the flow behaves essentially as a single-phase fountain. Our quantitative data in this regime are consistent with estimates from models of single-phase fountains in a crossflow, as described in [§ 3.2](#). In regime II, we observe the separation of some particles during the descent of the fountain which leads to a reduction in the dispersal distance of the particles. Finally, in regime III, when the fall speed of the particles is comparable to characteristic fountain speed $U > 1$, we show that the particles separate from the flow during the ascent of the fountain, which significantly reduces the dispersal distance of the particles.

Using our observations, we have shown that these regimes are not only a function of the dimensionless fall speed of the particles, U , but also a function of the dimensionless crossflow speed, P . The quantitative data presented in [§ 4.2](#) ([figures 8 and 9](#)) reveal that as the speed of the crossflow increases, particles of a smaller size separate from the fountain fluid and settle at their Stokes fall speed through the water column rather than remaining coupled to the fountain fluid. To justify this finding, in [figure 10](#) we present the magnitude of the vertical speed of a single-phase fountain for three different crossflow speeds as calculated from (3.10) and (3.11). Although these are theoretical curves, the model leads to centreline and radius profiles that provide a good fit to our experimental data, and this suggests that this model is an appropriate approximation for our experiments. These curves show that the vertical speed in the fountain decreases as the crossflow speed increases.

On particle fountains in a crossflow

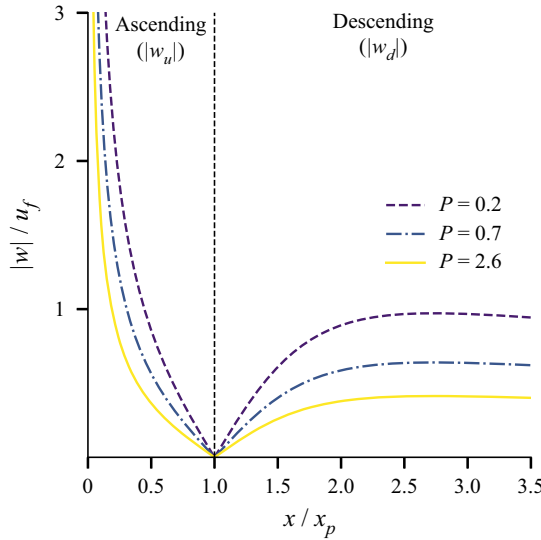


Figure 10. The magnitude of the vertical velocity along the fountain for three different crossflow speeds.

By considering a parcel of fluid in a single-phase fountain that follows the path given by (3.6) and (3.9), the total vertical distance travelled by this parcel of fluid is

$$2z_p \sim (h_m h_f^2)^{1/3}. \tag{5.1}$$

The total horizontal distance travelled by this parcel of fluid is given by the touchdown distance, x_t , which is found by substituting $z_d = 0$ into (3.9), and we find that

$$x_t \sim \frac{h_f^2}{h_m}. \tag{5.2}$$

Using (3.1), the vertical speed in the fountain is given by

$$w = \frac{dz}{dx} u_a \tag{5.3}$$

and, therefore, the average vertical speed of a parcel of fluid in the fountain is

$$|w| = \frac{2z_p}{x_t} u_a \sim \left(\frac{|B_0|^2}{M_0} \right)^{1/3} u_a^{-1/3} \tag{5.4}$$

and, hence, we find that the vertical speed in the fountain, $|w|$, is proportional to $u_a^{-1/3}$, where u_a is the speed of the crossflow.

For a particle to separate from the fountain fluid, we assume that the Stokes fall speed of that particle must exceed the magnitude of the vertical speed of the fountain, $v_s > |w|$. This assumption can be applied to particles that separate from the fountain during both the upflow and downflow regions of the fountain. Given that $|w| \sim u_a^{-1/3}$, the critical value of U at which $v_s > |w|$ and particle separation occurs scales as $u_a^{-1/3}$. Therefore, we expect that the critical values of the dimensionless fall speed, U_c , that delineate regimes I and II, at which particles separate during the downflow region of the fountain, and regimes II and III, at which particles separate during the upflow region of the fountain, depends on $P^{-1/3}$.

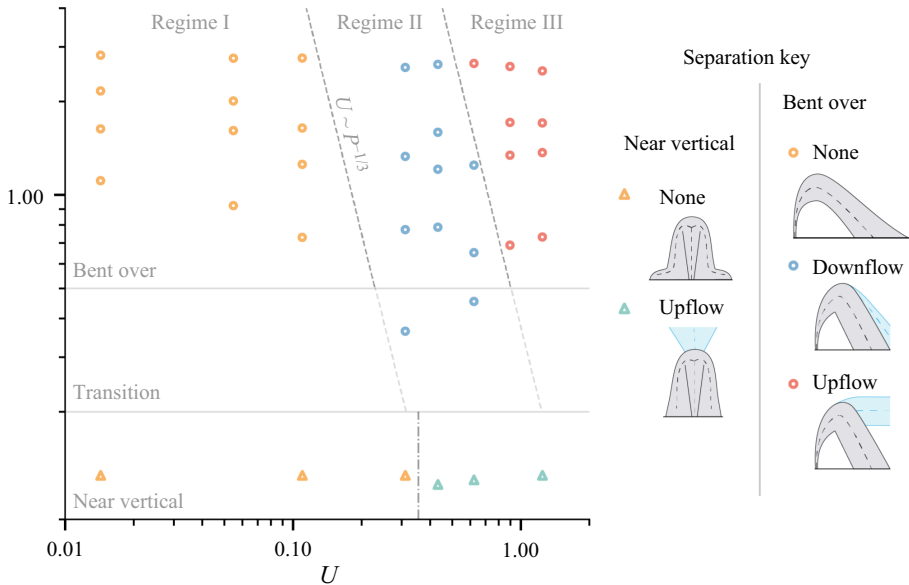


Figure 11. (a) Regime diagram displaying the separation regimes for particle-laden fountains in a crossflow showing the effect of the dimensionless crossflow speed, P , and the dimensionless fall speed of particles, U , on the dynamics of the flows. The diagonal dashed lines represent the transition between each separation regime and scale as $U \sim P^{-1/3}$, the horizontal solid lines represent the morphological regimes described in § 3.1.

To summarise the combined effects of both the dimensionless fall speed of the particles, U , and dimensionless crossflow speed, P , on the dynamics of particle-laden fountains, we now present the qualitative results of our experiments using a regime diagram (figure 11). Each experiment is represented by a point at its corresponding value of P and U , and coloured according to the separation regime observed for that experiment (§ 4.1). We have also included the qualitative regimes, as defined in § 3.1, to describe the effect of the crossflow on the morphology of the fountain. The separation of particles in the fountain is dependent on the particle size and, hence, fall speed of the particles. We see that in the region $0.1 < U < 1.0$, there is a transition in dynamics from a regime in which no particles separate from the flow (regime I), to a regime in which particles separate on the downflow (regime II) and finally particles separate during the ascent of the fountain (regime III). It is also evident from our regime diagram, and previous descriptions, that the point at which the particles separate from the fountain is also dependent on the speed of the crossflow. As described previously, we expect that the value of U at which particles separate from the flow scales as $P^{-1/3}$, therefore we have used this relationship to define the transitions between each regime in figure 11.

5.2. Application

Given the frequent appearance of particle-laden flows in the natural environment, the present work provides useful insight into the dynamics of these complex multiphase flows and how they interact with the ambient environment. Of particular interest is the evolution of deep-submarine explosive volcanic eruptions. In these eruptions, a mass flux of hot fragmented magma issues from a volcanic vent and mixes with a significant mass of cold seawater. After sufficient mixing, this flow becomes negatively buoyant and behaves as a multiphase fountain, consisting of a size distribution of pyroclasts and warm water, and the

On particle fountains in a crossflow

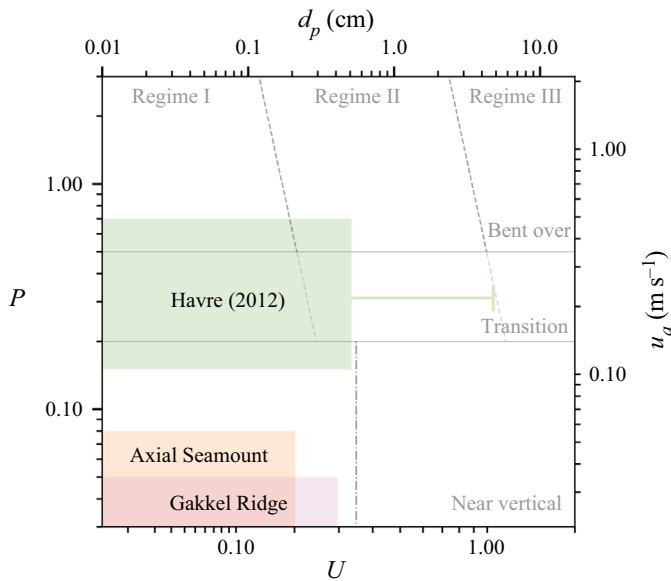


Figure 12. Regime diagram showing the effect of deep-ocean currents, u_a , and pyroclast diameter, d_p , on the dynamics of deep-submarine eruption. The following source conditions were used in the model presented in Newland *et al.* (2022) to simulate the conditions found at the Havre eruption of 2012 (Murch *et al.* 2020): vent depth = 1 km, vent radius = 3 m, initial velocity = 5 m s⁻¹, magma density = 2200 kg m⁻³ and magma temperature = 850 °C. The coloured boxes represent the range of measured pyroclast sizes and current speeds at the Havre 2012 eruption (Murch *et al.* 2020), the Axial Seamount and Gakkel Ridge (Barreyre, Soule & Sohn 2011), at which the deposits of deep-submarine eruptions have been studied.

subsequent dynamics of the flow will be affected by the conditions of the ambient water column, such as ocean currents (Head & Wilson 2003; Cas & Simmons 2018; Newland *et al.* 2022).

We can utilise the model presented in Newland *et al.* (2022) to calculate the conditions of an eruption column as it transitions to a negatively buoyant flow and, using the framework presented in this paper, we can describe how the magnitude of ocean currents and the size of pyroclasts may affect the eruption dynamics. In figure 12, using similar source conditions as presented in Murch *et al.* (2020), we illustrate how an eruption of similar size to the explosive stage of the 2012 eruption of the Havre Volcano may be affected by ambient currents. The coloured boxes represent the range of measured current speeds and pyroclast diameters for the Havre Volcano (Murch, White & Carey 2019; Murch *et al.* 2020) and, for comparison, the Axial Seamount (Barreyre *et al.* 2011) and Gakkel Ridge (Sohn *et al.* 2008; Pontbriand *et al.* 2012). To estimate the fall speed of the pyroclasts with varying diameter we follow the method of Ferguson & Church (2004) and Barreyre *et al.* (2011) and assume that the pyroclasts have a simplified spherical shape. This figure shows that the range of measured currents in the vicinity of the Havre Volcano are strong enough to lead to significant deflection of the eruption column and, owing to the size of pyroclasts observed, our regime diagram suggests that particle separation may play a critical role in defining the structure of the flow. As shown in § 4.2, this may lead to reduced dispersal distance of pyroclasts from the source. However, for an eruption of similar size at either the Axial Seamount or Gakkel Ridge, our work suggests that the dynamics of the flow would not be measurably altered.

It is important to note that, due to the technical and financial difficulties associated with studying the deposits of deep-submarine eruptions, the availability of comprehensive data sets is poor. Therefore, we expect that, given significant variations in the source conditions of eruptions such as vent depth and mass eruption rate, the dynamics explored in this study will be observed in the deep ocean and that the framework we have developed may help to interpret the deposits found on the seafloor.

6. Conclusions

In this work, we have presented a novel set of experiments that investigate the dynamics of particle-laden fountains in a uniform crossflow. We build a regime diagram to describe the effect of the dimensionless crossflow speed, P , and the dimensionless particle fall speed, U , on the structure and dynamics of these complex multiphase flows. By varying the dimensionless fall speed, U , of the particles we have identified three regimes that describe the dynamics of these flows. In regime I when $U < 0.1$, we find that the particles remain coupled to the fountain fluid and flow behaves essentially as a single-phase fountain in a crossflow. In the transitional regime II as $0.1 < U < 1.0$, we observe that particles separate from the flow during the descent of the fountain. Finally, in regime III when $U > 1.0$, the particles fall out of the flow during the ascent of the fountain and settle through the water column at a speed close to their Stokes fall speed. We have presented quantitative data on the dispersal distances and descent speed of particles and use a model of single-phase fountains in a crossflow (Chu 1975) to help describe the separation of particles from the fountain fluid. We have found that the critical value of U at which particle separation dominates the dynamics of the flow depends on the crossflow speed, such that $U_c \sim P^{-1/3}$. Finally, we have contextualised our study by using it as a framework to help interpret the deposits of deep-submarine explosive eruptions.

Funding. This work was supported by the Natural Environment Research Council (grant number 2261860).

Declaration of interests. The authors report no conflict of interest.

Author ORCIDs.

 Eric L. Newland <https://orcid.org/0000-0003-3501-8115>;

 Andrew W. Woods <https://orcid.org/0000-0002-5098-9940>.

Appendix. Comparison of fountain centreline estimates

To estimate the time-averaged centre of mass of a fountain, we follow the approach of James *et al.* (2022) who estimated the centre of mass of buoyant plumes in a crossflow by fitting Gaussian curves to vertical profiles of dye concentration along the length of the plume. In our experiments, we observe that as the fountain moves downstream and the horizontal flow speed downstream rapidly adjusts to the current speed, the vertical speed in the fountain becomes relatively small and therefore we expect that the centre and radius of the fountain can be tracked based on a vertical line through the flow. We test this assumption by tracking the radius and centreline of the flow along lines normal to the axis of the fountain, and compare these with the values of the radius and centreline as obtained from a vertical line through the fountain. For a typical example, we show the difference between these two approaches for a fountain with $P = 0.96$ in figure 13(a,b). In (c) we show a comparison of the two centreline measurements using these approaches, where it may be seen that there is very little difference between the two measurements. Finally, in (d) we show the root-mean-square errors between the measurement of the centreline as a

On particle fountains in a crossflow

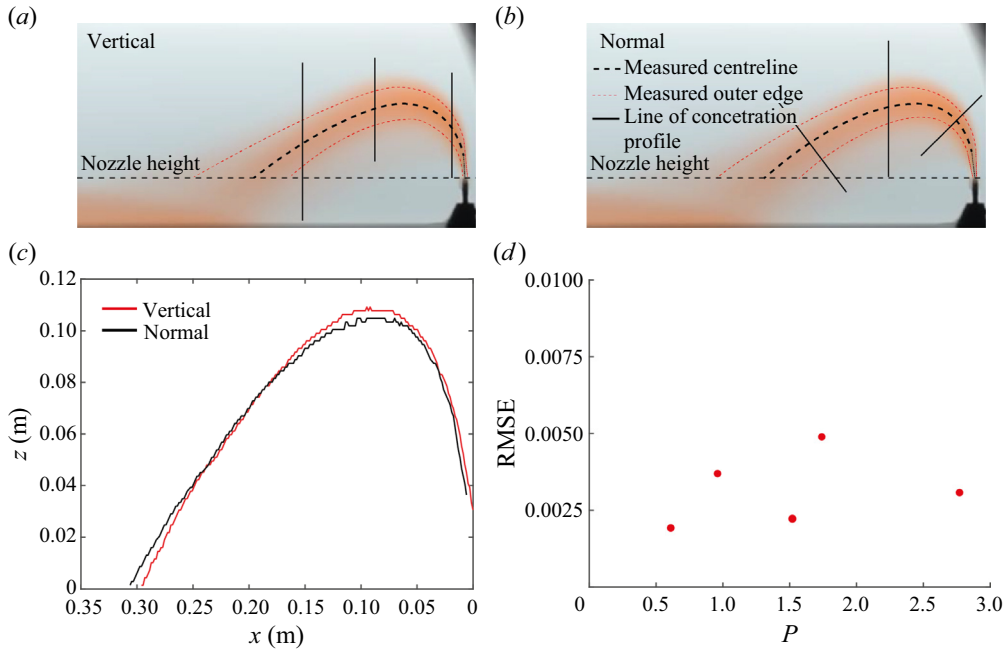


Figure 13. Time-averaged images from an experiment in which $P = 0.96$ with the measured centreline and radius superimposed, where a Gaussian has been fit to (a) the vertical concentration profiles and (b) the normal concentration profiles as shown by the black solid lines. (c) Comparison of the centreline measurements for vertical and normal Gaussian fits. (d) The root-mean-square error (RMSE) of the centreline estimates from the Gaussian fits to the vertical and normal concentration profiles for the single-phase fountains when $P > 0.5$, as a function of the dimensionless crossflow speed, P .

function of the distance downstream for the two approaches and we see there is very little difference between the results of these methods.

The Gaussian fits provide a good estimate of the centreline and radius for distances at least 1–2 cm beyond the source; however, directly above the source, the concentration profiles do not represent a Gaussian distribution. Therefore, we carry out a linear interpolation from the final readings of the centreline and radius to the nozzle location, represented by the dotted red and black lines near the source in figure 13(a,b).

REFERENCES

- ANDERSON, J.L., PARKER, F.L. & BENEDICT, B.A. 1973 Negatively buoyant jets in a cross flow. *Tech. Rep.* EPA-660/2-73-012. US Environmental Protection Agency.
- ANSONG, J.K., ANDERSON-FREY, A. & SUTHERLAND, B.R. 2011 Turbulent fountains in one-and two-layer crossflows. *J. Fluid Mech.* **689**, 254–278.
- AUBRY, T.J., JELLINEK, A.M., CARAZZO, G., GALLO, R., HATCHER, K. & DUNNING, J. 2017 A new analytical scaling for turbulent wind-bent plumes: comparison of scaling laws with analog experiments and a new database of eruptive conditions for predicting the height of volcanic plumes. *J. Volcanol. Geoth. Res.* **343**, 233–251.
- BAINES, W.D., TURNER, J.S. & CAMPBELL, I.H. 1990 Turbulent fountains in an open chamber. *J. Fluid Mech.* **212**, 557–592.
- BARREYRE, T., SOULE, S.A. & SOHN, R.A. 2011 Dispersal of volcanoclasts during deep-sea eruptions: settling velocities and entrainment in buoyant seawater plumes. *J. Volcanol. Geoth. Res.* **205** (3–4), 84–93.
- BEN MEFTAH, M., MALCANGIO, D., DE SERIO, F. & MOSSA, M. 2018 Vertical dense jet in flowing current. *Environ. Fluid Mech.* **18** (1), 75–96.

- BLOOMFIELD, L.J. & KERR, R.C. 2000 A theoretical model of a turbulent fountain. *J. Fluid Mech.* **424**, 197–216.
- BURRIDGE, H.C. & HUNT, G.R. 2012 The rise heights of low-and high-Froude-number turbulent axisymmetric fountains. *J. Fluid Mech.* **691**, 392–416.
- BURRIDGE, H.C. & HUNT, G.R. 2013 The rhythm of fountains: the length and time scales of rise height fluctuations at low and high Froude numbers. *J. Fluid Mech.* **728**, 91–119.
- CARAZZO, G., KAMINSKI, E. & TAIT, S. 2015 The timing and intensity of column collapse during explosive volcanic eruptions. *Earth Planet. Sci. Lett.* **411**, 208–217.
- CAS, R.A.F. & SIMMONS, J.M. 2018 Why deep-water eruptions are so different from subaerial eruptions. *Front. Earth Sci.* **6** (November), 1–21.
- CHOI, K.W., LAI, C.C.K. & LEE, J.H.W. 2016 Mixing in the intermediate field of dense jets in cross currents. *J. Hydraul. Engng* **142** (1), 04015041.
- CHU, V.H. 1975 Turbulent dense plumes in a laminar cross flow. *J. Hydraul. Res.* **13** (3), 263–279.
- CHU, V.H. & GOLDBERG, M.B. 1974 Buoyant forced-plumes in cross flow. *J. Hydraul. Div.* **100** (9), 1203–1214.
- CHU, V.H. & LEE, J.H.W. 1996 General integral formulation of turbulent buoyant jets in cross-flow. *J. Hydraul. Engng* **122** (1), 27–34.
- DEGRUYTER, W. & BONADONNA, C. 2013 Impact of wind on the condition for column collapse of volcanic plumes. *Earth Planet. Sci. Lett.* **377–378**, 218–226.
- DEVENISH, B.J., ROONEY, G.G. & THOMSON, D.J. 2010a Large-eddy simulation of a buoyant plume in uniform and stably stratified environments. *J. Fluid Mech.* **652**, 75–103.
- DEVENISH, B.J., ROONEY, G.G., WEBSTER, H.N. & THOMSON, D.J. 2010b The entrainment rate for buoyant plumes in a crossflow. *Boundary-Layer Meteorol.* **134** (3), 411–439.
- FAN, J.Y., XU, S.L. & WANG, D.Z. 2010 PDA measurements of two-phase flow structure and particle dispersion for a particle-laden jet in crossflow. *J. Hydrodyn.* **22** (1), 9–18.
- FERGUSON, R.I. & CHURCH, M. 2004 A simple universal equation for grain settling velocity. *J. Sedim. Res.* **74** (6), 933–937.
- GUNGOR, E. & ROBERTS, P.J.W. 2009 Experimental studies on vertical dense jets in a flowing current. *J. Hydraul. Engng* **135** (11), 935–948.
- HEAD III, J.W. & WILSON, L. 2003 Deep submarine pyroclastic eruptions: theory and predicted landforms and deposits. *J. Volcanol. Geoth. Res.* **121** (3–4), 155–193.
- HEWETT, T.A., FAY, J.A. & HOULT, D.P. 1971 Laboratory experiments of smokestack plumes in a stable atmosphere. *Atmos. Environ.* **5** (6), 767–789.
- HOULT, D.P., FAY, J.A. & FORNEY, L.J. 1969 A theory of plume rise compared with field observations. *J. Air Pollut. Control. Assoc.* **19** (8), 585–590.
- HOULT, D.P. & WEIL, J.C. 1972 Turbulent plume in a laminar cross flow. *Atmos. Environ.* **6**, 513–531.
- HUNT, G.R. & BURRIDGE, H.C. 2015 Fountains in industry and nature. *Annu. Rev. Fluid Mech.* **47** (1), 195–220.
- JAMES, C.B.G., MINGOTTI, N. & WOODS, A.W. 2022 On particle separation from turbulent particle plumes in a cross-flow. *J. Fluid Mech.* **932**, 1–15.
- KAYE, N.B. & HUNT, G.R. 2006 Weak fountains. *J. Fluid Mech.* **558**, 319–328.
- LEE, J.H. & CHU, V.H. 2003 *Turbulent Jets and Plumes: A Lagrangian Approach*, vol. 1. Springer Science & Business Media.
- MCDUGALL, T.J. 1981 Negatively buoyant vertical jets. *Tellus* **33** (3), 313–320.
- MEHADDI, R., VAUX, S., CANDELIER, F. & VAUQUELIN, O. 2015 On the modelling of steady turbulent fountains. *Environ. Fluid Mech.* **15** (6), 1115–1134.
- MICHAUD-DUBUY, A., CARAZZO, G. & KAMINSKI, E. 2020 Wind entrainment in jets with reversing buoyancy: implications for volcanic plumes. *J. Geophys. Res.* **125** (10), 1–18.
- MINGOTTI, N. & WOODS, A.W. 2016 On turbulent particle fountains. *J. Fluid Mech.* **793**, R1.
- MINGOTTI, N. & WOODS, A.W. 2019 Multiphase plumes in a stratified ambient. *J. Fluid Mech.* **869**, 292–312.
- MINGOTTI, N. & WOODS, A.W. 2020 Stokes settling and particle-laden plumes: implications for deep-sea mining and volcanic eruption plumes. *Phil. Trans. R. Soc.* **200** (part 2), 20190532.
- MINGOTTI, N. & WOODS, A.W. 2022 Dynamics of sediment-laden plumes in the ocean. *Flow* **2**, E26.
- MORTON, B.R., TAYLOR, J. & TURNER, J.S. 1956 Turbulent gravitational convection from maintained and instantaneous sources. *Proc. R. Soc. A* **234** (1196), 1–23.
- MURCH, A.P., WHITE, J.D.L., BARREYRE, T., CAREY, R.J., MUNDANA, R. & IKEGAMI, F. 2020 Volcaniclastic dispersal during submarine lava effusion: the 2012 eruption of Havre Volcano, Kermadec Arc, New Zealand. *Front. Earth Sci.* **8** (July), 1–21.

On particle fountains in a crossflow

- MURCH, A.P., WHITE, J.D.L. & CAREY, R.J. 2019 Characteristics and deposit stratigraphy of submarine-erupted silicic ash, Havre Volcano, Kermadec Arc, New Zealand. *Front. Earth Sci.* **7** (January), 1–21.
- NEWLAND, E.L., MINGOTTI, N. & WOODS, A.W. 2022 Dynamics of deep-submarine volcanic eruptions. *Sci. Rep.* **12**, 1–11.
- NEWLAND, E.L. & WOODS, A.W. 2021 On particle fountains in a stratified environment. *J. Fluid Mech.* **917**, 1–22.
- PARK, J. & PARK, H. 2021 Particle dispersion induced by vortical interactions in a particle-laden upward jet with a partial crossflow. *J. Fluid Mech.* **915**, A5.
- PINCINCE, A.B. & LIST, E.J. 1973 Disposal of brine into an estuary. *J. Water Pollut. Control Fed.* **45** (11), 2335–2344.
- PONTBRIAND, C.W., SOULE, S.A., SOHN, R.A., HUMPHRIS, S.E., KUNZ, C., SINGH, H., NAKAMURA, K.I., JAKOBSSON, M. & SHANK, T. 2012 Effusive and explosive volcanism on the ultraslow-spreading Gakkel Ridge, 85°E. *Geochem. Geophys. Geosyst.* **13** (10), 1–22.
- ROBERTS, P.J.W. & TOMS, G. 1987 Inclined dense jets in flowing current. *J. Hydraul. Engng* **113** (3), 323–341.
- ROWELL, C.R., JELLINEK, A.M., HAJIMIRZA, S. & AUBRY, T.J. 2022 External surface water influence on explosive eruption dynamics, with implications for stratospheric sulfur delivery and volcano-climate feedback. *Front. Earth Sci.* **10**, 788294.
- SLAWSON, P.R. & CSANADY, G.T. 1967 On the mean path of buoyant, bent-over chimney plumes. *J. Fluid Mech.* **28** (2), 311–322.
- SOHN, R.A., *et al.* 2008 Explosive volcanism on the ultraslow-spreading Gakkel Ridge, Arctic Ocean. *Nature* **453** (7199), 1236–1238.
- SUMNER, D., HESELTINE, J.L. & DANSEREAU, O.J.P. 2004 Wake structure of a finite circular cylinder of small aspect ratio. *Exp. Fluids* **37** (5), 720–730.
- TAHERIAN, M. & MOHAMMADIAN, A. 2021 Buoyant jets in cross-flows: review, developments, and applications. *J. Mar. Sci. Engng* **9** (1), 1–36.
- TURNER, J.S. 1973 *Buoyancy Effects in Fluids*. Cambridge University Press.
- TURNER, J.S. 1966 Jets and plumes with negative or reversing buoyancy. *J. Fluid Mech.* **26** (4), 779–792.
- WILLIAMSON, N., SRINARAYANA, N., ARMPFIELD, S.W., MCBAIN, G.D. & LIN, W. 2008 Low-Reynolds-number fountain behaviour. *J. Fluid Mech.* **608**, 297–317.
- WOODHOUSE, M.J., HOGG, A.J., PHILLIPS, J.C. & SPARKS, R.S.J. 2013 Interaction between volcanic plumes and wind during the 2010 Eyjafjallajökull eruption, Iceland. *J. Geophys. Res.* **118** (1), 92–109.
- WOODS, A.W. 2010 Turbulent plumes in nature. *Annu. Rev. Fluid. Mech.* **42** (1), 391–412.
- ZHANG, H. & BADDOUR, R.E. 1998 Maximum penetration of vertical round dense jets at small and large Froude numbers. *J. Hydraul. Engng* **124** (5), 550–553.